

Swin UNETR++: Advancing Transformer-Based Dense Dose Prediction Towards Fully Automated Radiation Oncology Treatments

Kuancheng Wang

Georgia Institute of Technology, Atlanta, GA, USA

KWANG601@GATECH.EDU

Hai Siong Tan

Department of Radiation Oncology, Perelman School of Medicine, University of Pennsylvania, Philadelphia, PA, USA

HAISIONG.TAN@PENNMEDICINE.UPENN.EDU

Rafe Mcbeth

Department of Radiation Oncology, Perelman School of Medicine, University of Pennsylvania, Philadelphia, PA, USA

RAFE.MCBETH@PENNMEDICINE.UPENN.EDU

Abstract

The field of Radiation Oncology is uniquely positioned to benefit from the use of artificial intelligence to fully automate the creation of radiation treatment plans for cancer therapy. This time-consuming and specialized task combines patient imaging with organ and tumor segmentation to generate a 3D radiation dose distribution to meet clinical treatment goals, similar to voxel-level dense prediction. In this work, we propose Swin UNETR++, that contains a lightweight 3D Dual Cross-Attention (DCA) module to capture the intra and inter-volume relationships of each patient's unique anatomy, which fully convolutional neural networks lack. Our model was trained, validated, and tested on the Open Knowledge-Based Planning dataset. In addition to metrics of Dose Score $\overline{S_{Dose}}$ and DVH Score $\overline{S_{DVH}}$ that quantitatively measure the difference between the predicted and ground-truth 3D radiation dose distribution, we propose the qualitative metrics of average volume-wise acceptance rate $\overline{R_{VA}}$ and average patient-wise clinical acceptance rate $\overline{R_{PA}}$ to assess the clinical reliability of the predictions. Swin UNETR++ demonstrates near-state-of-the-art performance on validation and test dataset (validation: $\overline{S_{DVH}}=1.492$ Gy, $\overline{S_{Dose}}=2.649$ Gy, $\overline{R_{VA}}=88.58\%$, $\overline{R_{PA}}=100.0\%$; test: $\overline{S_{DVH}}=1.634$ Gy, $\overline{S_{Dose}}=2.757$ Gy, $\overline{R_{VA}}=90.50\%$, $\overline{R_{PA}}=98.0\%$), establishing a basis for future studies to translate 3D dose predictions into a deliverable treatment plan, facilitating full automation.

Keywords: Radiation Dense Dose Prediction, Vision Transformer, Swin UNETR++, Dual Cross-Attention

1. Introduction

Radiotherapy remains a critical tool in the fight against cancer, employing sophisticated techniques like intensity-modulated radiation therapy (IMRT) for precise radiation delivery. Yet, even as artificial intelligence (AI) has emerged to assist with organ segmentation in the clinic, the development of patient-specific treatment plans remains a highly complicated and time-consuming task that lies outside the reach of current AI-based approaches. This complexity originates from trade-off decisions that must balance the maximum radiation dose to the tumor while minimizing the dose to surrounding normal tissues. Furthermore, converting physician treatment plan intent to deliverable linear accelerator or “robot” sequenced motions involves solving a complex inverse optimization problem using proprietary simulated annealing algorithms within dedicated treatment planning systems. To address this problem, several groups have worked to develop techniques to translate anatomical information, i.e., 3D images and associated organ segmentation, to a predicted radiation dose distribution that matches clinical constraints (Liu et al., 2021a; Nguyen et al., 2019c). Competitions such as Open Knowledge-Based Planning Grand Challenge (OpenKBP) (Babier et al., 2021) have been initiated to challenge the community to make progress on this problem, but current approaches still depend on fully convolutional models that may not be sufficient for generating deliverable treatment plans due to the lack of large receptive fields. The goal of this work is to transition fully convolutional 3D dose prediction to attention-based.

We introduced Swin UNETR++, a novel deep learning architecture that aims to supplant the extant fully convolutional neural network (FCNN) approaches in 3D dose prediction. This new model is backboneed by Swin UNETR (Hatamizadeh et al., 2021) and incorporates a lightweight 3D Dual Cross-Attention (DCA) module designed to bridge the semantic gap between encoder and decoder features in the skip connection. This architecture excels at capturing both channel and spatial dependencies, thereby providing a more holistic view of the patient’s anatomy for accurate dose prediction. Swin UNETR++ was rigorously evaluated using the OpenKBP dataset and trained using a hybrid of mean squared error loss \mathcal{L}_{MSE} and a novel global differentiable approximation of the dose-volume histogram loss $\mathcal{L}_{\text{DVH_global}}$. In terms of performance metrics, Swin UNETR++ shows near-state-of-the-art results, outpacing most existing models in both the validation and test phases, and its implementation marks a significant advancement in automating the radiotherapy planning process. This study not only outlines the architecture and performance of Swin UNETR++ but also opens avenues for further research in incorporating more nuanced attention mechanisms into treatment planning.

2. Related Work

After the OpenKBP dataset was released, several teams have shown the strength of full CNN. Nguyen et al. (2019b) proposed Hierarchically Densely Connected U-net (HD U-net). Soomro et al. (2021) introduced DeepDoseNet, which integrates Resnet (He et al., 2016) and dilated densenet blocks in their architecture. Liu et al. (2021a) proposed cascade 3D model, C3D, which ranked No.1 on OpenKBP leaderboard for both $\overline{S}_{\text{DVH}}$ and $\overline{S}_{\text{Dose}}$. In C3D, two U-nets are connected in series, and the second U-net refines the coarse prediction made by the first U-net. As ViT (Dosovitskiy et al., 2020) and Swin UNETR result in state-of-the-art performance in classification and segmentation tasks, we use Swin UNETR++ to demonstrate the superiority of the transformer-based approach in 3D radiation dose estimation.

3. Method

3.1. Dataset

The OpenKBP dataset contains 340 patients treated by IMRT for head-and-neck cancer. Each patient was prescribed a combination of three possible radiation doses: 70 Gy to the gross disease planning target volume (PTV70), 63 Gy to the intermediate-risk planning target volumes (PTV63), and 56 Gy to the elective planning target volumes (PTV56), with organs-at-risk (OARs) masks including the brain stem, spinal cord, right parotid, left parotid, esophagus, larynx, and mandible. In addition, CT, the ground-truth 3D radiation dose distribution, and a possible dose mask contouring the body are provided for each patient. All image data are downsampled to $128 \times 128 \times 128$ voxels with voxel dimensions around $3.5 \text{ mm} \times 3.5 \text{ mm} \times 2 \text{ mm}$. In terms of dataset distribution, OpenKBP Grand Challenge assigned patients No.1–200 for training, No.201–240 for validation, and No.241–340 for testing.

3.2. Model Architecture

3.2.1. SWIN UNETR

Swin UNETR has recently emerged as a promising method for medical image segmentation challenges, registering state-of-the-art performance in specialized domains such as glioma delineation, Medical Segmentation Decathlon (Simpson et al., 2019), and Beyond The Cranial Vault Segmentation Challenge (Tang et al., 2022). The model combines the computational advantages of the Swin Transformer (Liu et al., 2021b), known for its shifted window attention mechanisms with the domain-specific robustness of UNETR (Hatamizadeh et al., 2022). This combination benefits from spatial hierarchy representation but also adheres to computational efficiency guidelines. However, despite these merits, our analysis has identified an overlooked shortcoming—namely, the semantic gap between the encoder and decoder features propagated through the skip connections. The discrepancies between low-level features and high-level semantics in U-Net-based architectures are corroborated by Pang et al. (2019) and Wang et al. (2022). Resolving this semantic inconsistency could improve the accuracy of 3D radiation dose prediction, which requires more details and clinical understanding than semantic segmentation.

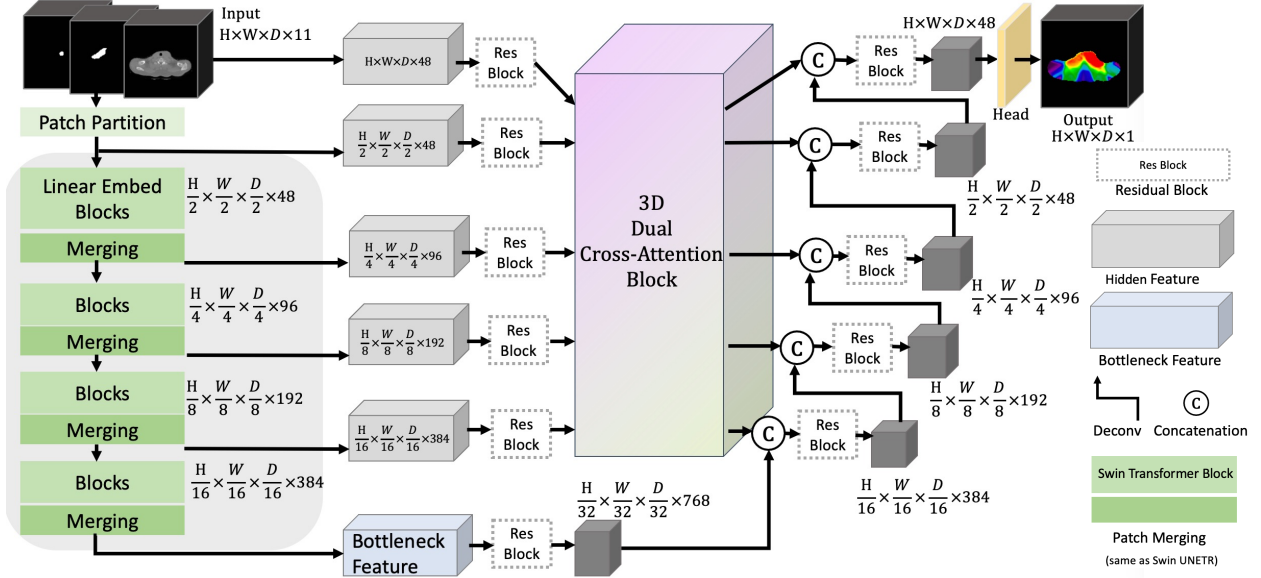


Figure 1: Swin UNETR++ model architecture highlighting 3D dual cross-attention (DCA) module

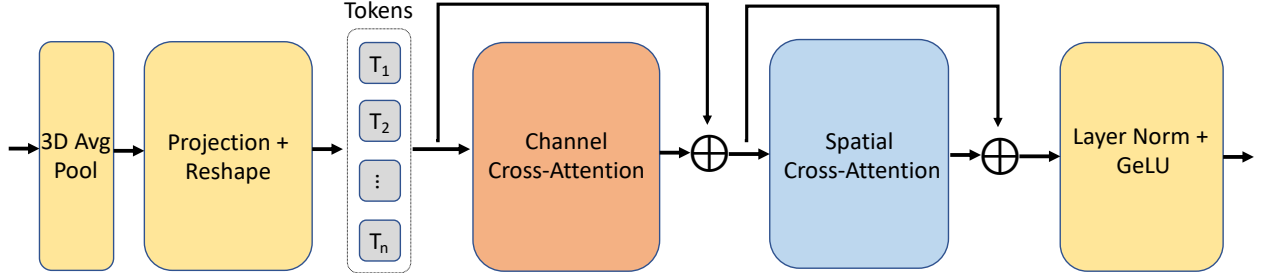


Figure 2: DCA module internal structure

3.2.2. SWIN UNETR++

Research has been looking at using attention mechanisms to improve the performance of U-Net-based architectures. For instance, Mou et al. (2021) introduced CS²-Net, which utilized spatial and channel attention to facilitate the segmentation of curvilinear structures. The DANet (Fu et al., 2019) integrated position and channel attention module in scene segmentation. Recently, Ates et al. (2023) proposed a light-weight 2D plug-and-play Dual Cross-Attention (DCA) module which has demonstrated its efficiency in reducing the semantic gap among common fully convolutional U-Net-based architecture.

In extending the conventional 2D DCA module to 3D, the fundamental operations, such as convo-

lutional layers, pooling operations, and batch normalization, have been extended from 2D to their 3D counterparts. It comprises three essential stages: multi-scale 3D patch embedding, a 3D Channel Cross-Attention (CCA) module, and a 3D Spatial Cross-Attention (SCA) module.

3D Patch Embedding. We used the same patch size defined by Ates et al. (2023). Given n encoder stages and encoder features $E_i \in \mathbb{R}^{C_i \times \frac{H}{2^{i-1}} \times \frac{W}{2^{i-1}} \times \frac{D}{2^{i-1}}}$ where $i \in \{1, 2, \dots, n\}$, the flattened patches for stage i are extracted by 3D $1 \times 1 \times 1$ depth-wise convolutions and 3D average pooling layer as following:

$$T_i = \text{DConv1D}_{E_i}(\text{Reshape}(\text{AvgPool3D}_{E_i}(E_i))) \quad (1)$$

3D Channel Cross-Attention (CCA) module. We concatenated T_i along the channel dimension to create T_c . By using the 3D $1 \times 1 \times 1$ depth-wise convolutions, we can obtain the queries Q_i , projected keys K , values V , and CCA as follows:

$$Q_i = \text{DConv1D}_{Q_i}(T_i) \quad (2)$$

$$K = \text{DConv1D}_K(T_c) \quad (3)$$

$$V = \text{DConv1D}_V(T_c) \quad (4)$$

$$C_c = \text{total num of channels} \quad (5)$$

$$\text{CCA}(Q_i, K, V) = \text{Softmax} \left(\frac{Q_i^T K}{\sqrt{C_c}} \right) V^T \quad (6)$$

3D Spatial Cross-Attention (SCA) module. With the reshaped output from CCA \bar{T}_i , we can obtain \bar{T}_c by layer normalization and channel concatenation. Similarly, we can obtain the queries Q_i , keys K , values V , and SCA as follows:

$$Q = \text{DConv1D}_Q(\bar{T}_i) \quad (7)$$

$$K = \text{DConv1D}_K(\bar{T}_c) \quad (8)$$

$$V_i = \text{DConv1D}_{V_i}(\bar{T}_i) \quad (9)$$

$$h = \text{num of heads for CCA} \quad (10)$$

$$\text{SCA}(Q, K, V_i) = \text{Softmax} \left(\frac{Q K^T}{\sqrt{\frac{C_c}{h}}} \right) V_i \quad (11)$$

By combining the 3D DCA module in Figure 2 with the Swin UNETR architecture in the skip connection, we proposed Swin UNETR++ illustrated in Figure 1. It improves medical image analysis and is specifically tailored for dense radiation dose prediction. It is also the first time the 3D DCA module was applied outside semantic segmentation.

The 3D DCA module has clinical importance as well. CCA refines the model’s understanding of the channel-wise relationship between different clinically significant volumes, similar to the prior work of overlap volume histogram (Wu et al., 2009) that quantified the distance between different OARs and PTVs. SCA establishes the close-and-distant relationships within each clinically significant volume. Together, CCA and SCA aim to heighten treatment efficacy while minimizing radiation-induced complications, contributing to a safer, more effective therapeutic regimen.

3.3. Network Training

3.3.1. DATA PREPROCESSING AND AUGMENTATION

Inspired by Liu et al. (2021a), we first clipped the CT images into a fixed range between -1024 and 1500 HU and then normalized them by 1000 HU during preprocessing. Any missing volume masks for each patient are represented by a 3D zero tensor.

During training, we applied data augmentation with MONAI (Cardoso et al., 2022) to increase our model’s generalizability and avoid overfitting in the following order: (1)Random axis flip which randomly flips the spatial axis of CT, structured masks, and possible dose mask (probability=0.5). (2)Random affine which performs random shearing in a range of (0.1, 0.1, 0.1) with zero-padding and nearest-neighbor interpolation on CT, structured masks, and possible dose mask (probability=0.2). (3)Random zoom scales CT, structured masks, and possible dose mask within a range of [0.9, 1.3] with nearest-neighbor interpolation (probability=0.5). (4)Random Gaussian smooth is applied only to CT (probability=0.2). (5)Random contrast is applied only to CT (probability=0.2).

3.3.2. LOSS FUNCTION

To compare the voxel difference between the predicted radiation dose distribution D_{pred} and the ground-truth radiation dose distribution D_{gt} , the mean squared error (MSE) was used due to its sensitivity to outliers. Therefore, we designed the loss function \mathcal{L}_{MSE} , which only focuses on the dose difference within the patient’s body, using the possible dose mask M_d . For all possible voxel indices i, j, k :

$$\begin{aligned} \mathcal{L}_{\text{MSE}}(D_{\text{pred}}, D_{\text{gt}}) & \quad (12) \\ &= \frac{\sum_{i,j,k} (D_{\text{pred}}(i, j, k) - D_{\text{gt}}(i, j, k))^2 M_d(i, j, k)}{\sum_{i,j,k} M_d(i, j, k)} \end{aligned}$$

The DVH loss \mathcal{L}_{DVH} (Nguyen et al., 2020) is a loss function that takes into account a common clinical tool for assessing the dose to each organ in a treatment plan, the dose volume histogram (DVH). As the traditional DVH calculation is not differentiable, a differentiable approximate dose-volume histogram $\widetilde{\text{DVH}}$ is used. Given a set of n_v clinically significant volume masks M_v , where $v \in V = \text{PTV} \cup \text{OAR}$, and

the number of bins n_t , we can obtain:

$$\begin{aligned} \mathcal{L}_{\text{DVH}}(D_{\text{pred}}, D_{\text{gt}}, M_v) \\ = \frac{\sum_{v \in V} \|\widetilde{\text{DVH}}_v(D_{\text{gt}}, M_v) - \widetilde{\text{DVH}}_v(D_{\text{pred}}, M_v)\|_2^2}{n_v n_t} \end{aligned} \quad (13)$$

We introduced a variant of the DVH loss, the global DVH loss $\mathcal{L}_{\text{DVH_global}}$. The global DVH condenses the integral dose across the patient, i.e., the possible dose mask segmentation M_d , to a single line on the DVH plot. The loss then considers the difference of this integral dose distribution between the predicted and ground truth distributions. This loss considers the radiation dose across the entire patient's body as opposed to individual clinically segmented volumes that are sparse and account for only a fraction of the total patient volume. $\mathcal{L}_{\text{DVH_global}}$ is computed as follows:

$$\begin{aligned} \mathcal{L}_{\text{DVH_global}}(D_{\text{pred}}, D_{\text{gt}}, M_d) \\ = \frac{\|\widetilde{\text{DVH}}_v(D_{\text{gt}}, M_d) - \widetilde{\text{DVH}}_v(D_{\text{pred}}, M_d)\|_2^2}{n_t} \end{aligned} \quad (14)$$

We combined \mathcal{L}_{MSE} and $\mathcal{L}_{\text{DVH_global}}$ together as the final loss function for training :

$$\mathcal{L}_{\text{combined}} = \alpha \mathcal{L}_{\text{MSE}} + \beta \mathcal{L}_{\text{DVH_global}} \quad (15)$$

where both α and β were set to 10 empirically.

3.3.3. HYPERPARAMETER SETTING

Adam optimizer (Kingma and Ba, 2014) was initialized with a learning rate of 2e-4 and beta values of (0.5, 0.999). To adaptively adjust the learning rate during the training process, we utilized the Cosine Annealing with Warm Restarts scheduler. The initial restart period was set to 100 epochs, with a multiplicative factor of 1 and a minimum learning rate of 2e-5. Furthermore, we fixed the seed to 42, thereby ensuring deterministic behavior for stochastic operations and facilitating experiment reproducibility.

4. Evaluation Metrics

4.1. Quantitative Metrics

4.1.1. DOSE SCORE

Provided by OpenKBP, the Dose Score $\overline{S}_{\text{Dose}}$ is the mean absolute difference between the predicted radiation dose distribution D_{pred} and the ground-truth radiation dose distribution D_{gt} based on the possible

dose mask M_d for each patient P_t in either validation or test datasets.

$$\begin{aligned} \text{Error}_{\text{Dose}}(P_t) \\ = \frac{\sum_{i,j,k} |D_{\text{pred}}(i, j, k) - D_{\text{gt}}(i, j, k)| M_d(i, j, k)}{\sum_{i,j,k} M_d(i, j, k)} \end{aligned} \quad (16)$$

$$\overline{S}_{\text{Dose}} = \frac{1}{n} \sum_{t=1}^n \text{Error}_{\text{Dose}}(P_t) \quad (17)$$

4.1.2. DVH SCORE

DVH Score $\overline{S}_{\text{DVH}}$ (Babier et al., 2021) is designed to measure the quality of the predicted radiation dose distribution clinically. The radiation dose distribution for each OAR is evaluated by:

$D_{0.1cc}$:=The minimum max dose to all but 0.1cc
 D_{mean} :=The mean dose (i.e., the area under DVH curve)

The radiation dose distribution for each PTV is evaluated by:

D_1 :=The minimum max dose received by 99% of the target (i.e., 99th percentile)
 D_{95} :=The minimum dose received by 95% of the target (i.e., 5th percentile)
 D_{99} :=The minimum dose received by 99% of the target (i.e., 1st percentile)

Finally, the mean absolute difference between the predictions and the ground truth radiation dose distributions is computed based on the above metrics for each patient using their existing OAR and PTV masks.

4.2. Qualitative Metrics

To evaluate the clinical reliability of the model's predictions, we defined the absolute difference between the ground-truth and predicted dose distribution within 3 Gy as clinically acceptable and the absolute difference outside this range as clinically unacceptable (Sher et al., 2021; Mashayekhi et al., 2021).

4.2.1. VOLUME-WISE CLINICAL ACCEPTANCE

We consider the predicted radiation dose distribution for a volume to be volume-wise clinically acceptable VA if and only if the absolute dose distribution difference between the predicted and the ground-truth

within the given volume is less than 3 Gy. The function $VA()$ has two possible outputs: 1 represents volume-wise clinically acceptable while 0 represents unacceptable. Given a set of validation or test patients P and a set of clinically significant volumes V , the volume-wise clinical acceptance rate R_{VA} for a volume $v \in V$ is defined as:

$$R_{VA}(v) = \frac{1}{|P|} \sum_{p \in P} VA(p, v) \quad (18)$$

The average volume-wise clinical acceptance rate $\overline{R_{VA}}$ for an entire validation or test dataset is defined as:

$$\overline{R_{VA}} = \frac{1}{|V|} \sum_{v \in V} R_{VA}(v) \quad (19)$$

4.2.2. PATIENT-WISE CLINICAL ACCEPTANCE

Clinically, medical dosimetrists try to achieve Pareto optimal plans given individual patient’s unique anatomy and physicians’ prioritization, but different prioritization can lead to different “optimal” plans (Nguyen et al., 2019a; Kyroudi et al., 2020). To simulate these real-world plan variations, we first find the absolute difference between the predicted and ground-truth radiation dose distribution for all clinically significant volumes V of each patient p and then average those absolute differences. We consider a patient to be patient-wise clinically acceptable PA if and only if the average difference is less than 3 Gy. The function $PA()$ has two possible outputs: 1 represents patient-wise clinically acceptable while 0 represents patient-wise clinically unacceptable. Given a set of all validation or test patients P , the average patient-wise clinical acceptance rate $\overline{R_{PA}}$ for an entire validation or test dataset is defined as:

$$\overline{R_{PA}} = \frac{1}{|P|} \sum_{p \in P} PA(p, V) \quad (20)$$

5. Results

We compared the Swin UNETR’s performance with 3D U-Net (Çiçek et al., 2016), Attention U-Net (Oktay et al., 2018), SegResNet (Myronenko, 2019), DynUNet, HD U-net (Nguyen et al., 2019b), C3D (Liu et al., 2021a) and its backbone architecture Swin UNETR (Hatamizadeh et al., 2021). 3D U-Net, Attention U-Net, SegResNet, DynUNet, HD U-net, and C3D are fully CNN-based, among which HD U-net

and C3D are specifically designed for 3D radiation dose estimation. The training pipeline for all architectures is the same, except we modified the loss function for C3D to adapt its cascade mechanism. The architecture results measured based on $\overline{S_{DVH}}$, $\overline{S_{Dose}}$, $\overline{R_{VA}}$, and $\overline{R_{PA}}$ are available in Table 1, where the highest values of each metric in each dataset are highlighted. The details of these results are explained in sections 5.1 and 5.2 from the aspect of ablation study and clinical analysis.

5.1. Ablation Study

It’s clear from Table 1 that Swin UNETR++ outperforms all seven other architectures on $\overline{S_{DVH}}$, $\overline{S_{Dose}}$, $\overline{R_{VA}}$, and $\overline{R_{PA}}$ in both validation and test datasets. The only exception is HD U-net’s validation $\overline{R_{VA}}$ is 2.7% higher than Swin UNETR++’s. Out of 50 more teams, Swin UNETR++ should rank 1st on $\overline{S_{DVH}}$ and 9th on $\overline{S_{Dose}}$ in the validation dataset; ranks 12th on $\overline{S_{DVH}}$ and 10th on $\overline{S_{Dose}}$ in the test dataset on the leaderboard.

5.1.1. THE EFFECT OF 3D DCA MODULE

By comparing the metric scores between Swin UNETR++ and Swin UNETR in Table 1, Swin UNETR++ lowers $\overline{S_{DVH}}$ by 0.063 Gy and lowers $\overline{S_{Dose}}$ by 0.018 Gy in the validation dataset; lowers $\overline{S_{DVH}}$ by 0.139 Gy, $\overline{S_{Dose}}$ by 0.061 Gy, increases $\overline{R_{VA}}$ by 1.56%, and increases $\overline{R_{PA}}$ by 1% in the test dataset. This demonstrates the performance improvement due to the 3D DCA module.

5.1.2. THE EFFECT OF $\mathcal{L}_{MSE} + \mathcal{L}_{DVH_global}$

We further examined the advantage of the global DVH loss \mathcal{L}_{DVH_global} over the traditional DVH loss \mathcal{L}_{DVH} , which only calculates the structural DVH different based on the PTV and OAR masks, in table 2. These two loss functions are examined on test data since there are more variations in patients’ imaging, thus allowing us to better generalize the effect of \mathcal{L}_{DVH_global} . \mathcal{L}_{DVH_global} demonstrates its efficiency by lowering $\overline{S_{DVH}}$ by 0.157 Gy and lowering $\overline{S_{Dose}}$ by 0.159 Gy.

5.2. Clinical Analysis

We further investigated the potential clinical value Swin UNETR++ has. Figure 3 and 4 visualize each model’s dose estimation and its absolute difference

Table 1: Swin UNETR++ vs Baseline Models in terms of $\overline{S_{DVH}}$, $\overline{S_{Dose}}$, $\overline{R_{VA}}$, and $\overline{R_{PA}}$

Architecture	Dataset	$\overline{S_{DVH}}$	$\overline{S_{Dose}}$	$\overline{R_{VA}}$	$\overline{R_{PA}}$
Swin UNETR++	Validation	1.492	2.649	88.58%	100.00%
	Test	1.634	2.757	90.50%	98.00%
Swin UNETR	Validation	1.555	2.667	89.30%	100.00%
	Test	1.773	2.818	88.94%	97.00%
3D U-Net	Validation	2.763	3.325	68.34%	82.50%
	Test	2.778	3.408	70.07%	74.00%
Attention U-Net	Validation	2.035	2.868	86.23%	97.50%
	Test	2.079	3.044	83.19%	94.00%
SegResNet	Validation	2.029	2.858	79.69%	95.00%
	Test	1.987	2.941	84.19%	93.00%
DynUNet	Validation	2.252	3.028	82.45%	92.50%
	Test	2.222	3.096	85.87%	96.00%
HD U-Net	Validation	1.720	2.835	91.28%	100.00%
	Test	1.876	3.003	87.86%	97.00%
C3D	Validation	1.784	2.727	86.91%	95.00%
	Test	1.847	2.879	87.66%	96.00%

Table 2: Comparison between different combinations of loss functions

Architecture	Loss Function	Dataset	$\overline{S_{DVH}}$	$\overline{S_{Dose}}$
Swin UNETR++	\mathcal{L}_{DVH_global} & \mathcal{L}_{MSE}	Test	1.634	2.757
	\mathcal{L}_{DVH} & \mathcal{L}_{MSE}	Test	1.791	2.916

from ground truth on the same slice for the representative patient No.241 in the test dataset. Swin UNETR++ has higher accuracy in the high-dose volume, PTV56, PTV63, and PTV70, among other architectures. Figure 5 illustrates the dose-volume histogram for each architecture’s prediction on patient No.241. Unlike other architectures, Swin UNETR++ keeps the DVH-differences smallest among all regions of interest and never overdoses the PTVs, meaning it is comparatively safer.

The clinical reliability of the AI-generated plan is another major concern. While Table 1 provided the averaged volume acceptance rate $\overline{R_{VA}}$ and patient acceptance rate $\overline{R_{PA}}$, more details about the radiation dose distribution of each architecture for each volume in validation and test datasets can be found in Tables 3 and 4. Swin UNETR++ has a higher $\overline{R_{VA}}$ and $\overline{R_{PA}}$, highlighting its reliability. It’s also worth noting that there is no single model good at dose estimation for all the volumes of interest, indicating a possible improvement in the future.

6. Discussion

This work represents continued efforts to bridge the gap between the technical achievements of computer science and the complexities of clinical medicine. Adopting AI in radiation oncology requires clinical endpoints to be at the forefront of collaborations between the different domains. Replacing humans in clinical workflows with artificial intelligence is not appropriate from many patients’ perspectives, and instead, we believe these models will augment the clinical judgment and intelligence of clinical providers. While our results are not state-of-the-art on the specified OpenKBP grand challenge, the difference between the top ten models is very small, and each teams’ training pipeline is significantly different. For example, the No.1 team C3D iterated over each training patient multiple times in each epoch while we only iterated over each training patient once. We also don’t know if some teams used their own patient data to pretrain the model. Based on the experiment we did in section 5, our Swin UNETR has better performance than other models such as C3D (Liu et al.,

2021a) and is still representative of a model with clinical viability.

The competition dataset also does not fully represent the data in our clinic, as it contains IMRT plans that use static angles, whereas many clinics have transitioned to the use of volumetric modulated arc therapy (VMAT) plans that represent treatment along continuous arcs. Our clinical data represents more patients, has higher resolutions, contains more organ segmentations, represents our unique patient population, and is more variable in treatment approach than the idealized challenge data. We recognize that this work could benefit from additional clinical testing, but the scope of this project was limited to a summer undergraduate research fellowship. Further clinical training and testing are underway and will provide additional results.

Our model, which translates patient anatomy via CT images and associated segmentations to a 3D dose distribution, is the first step in a two-step process to produce a clinically deliverable radiation treatment plan. The second step involves generating treatment machine path sequences, i.e., multileaf collimator leaf sequences, gantry and collimator positions, etc., from the predicted 3D dose distributions. This step is currently solved by proprietary inverse optimization algorithms as described in (Otto, 2008) that require time-consuming manual intervention but may be solvable with more robust deep learning architectures, as shown in (Heilemann et al., 2023). This provided additional motivation for exploring the techniques described in this paper for future studies. If realized, finding solutions to the radiation treatment planning challenge will represent a large leap forward in the speed of creation and quality of treatment plans, augmenting treatment teams’ intelligence and maximizing efficiency.

7. Conclusion

In this paper, we introduced Swin UNETR++ which is a novel transformer-based architecture for dense radiation dose prediction. It integrates the dual cross-attention module, consisting of channel cross-attention and spatial cross-attention, into Swin UNETR’s skip connection to reduce the semantic gap between encoder and decoder features and capture significant clinical relationships between PTVs and OARs. Our model is examined on OpenKBP Grand Challenge dataset and demonstrates near-state-of-the-art performance on \overline{S}_{DVH} and \overline{S}_{Dose} . Further-

more, the investigation on the clinical safety and reliability of the prediction results confirms the potential clinical value transformer-based architecture can have. We believe that transitioning dose prediction from fully convolutional to transformer-based architectures will provide a strong foundation for the future work of translating dose prediction into deliverable treatment machine parameters, completing the full integration of AI into the clinical treatment planning process.

8. Acknowledgment

This work was supported by NIH grant R25 CA140116.

References

- Gorkem Can Ates, Prasoon Mohan, and Emrah Celik. Dual cross-attention for medical image segmentation. *arXiv preprint arXiv:2303.17696*, 2023.
- Aaron Babier, Binghao Zhang, Rafid Mahmood, Kevin L Moore, Thomas G Purdie, Andrea L McNiven, and Timothy CY Chan. Openkbp: the open-access knowledge-based planning grand challenge and dataset. *Medical Physics*, 48(9):5549–5561, 2021.
- M Jorge Cardoso, Wenqi Li, Richard Brown, Nic Ma, Eric Kerfoot, Yiheng Wang, Benjamin Murrey, Andriy Myronenko, Can Zhao, Dong Yang, et al. Monai: An open-source framework for deep learning in healthcare. *arXiv preprint arXiv:2211.02701*, 2022.
- Özgün Çiçek, Ahmed Abdulkadir, Soeren S Lienkamp, Thomas Brox, and Olaf Ronneberger. 3d u-net: learning dense volumetric segmentation from sparse annotation. In *Medical Image Computing and Computer-Assisted Intervention—MICCAI 2016: 19th International Conference, Athens, Greece, October 17–21, 2016, Proceedings, Part II 19*, pages 424–432. Springer, 2016.
- Alexey Dosovitskiy, Lucas Beyer, Alexander Kolesnikov, Dirk Weissenborn, Xiaohua Zhai, Thomas Unterthiner, Mostafa Dehghani, Matthias Minderer, Georg Heigold, Sylvain Gelly, et al. An image is worth 16x16 words: Transformers for image recognition at scale. *arXiv preprint arXiv:2010.11929*, 2020.
- Jun Fu, Jing Liu, Haijie Tian, Yong Li, Yongjun Bao, Zhiwei Fang, and Hanqing Lu. Dual attention network for scene segmentation. In *Proceedings of the IEEE/CVF conference on computer vision and pattern recognition*, pages 3146–3154, 2019.
- Ali Hatamizadeh, Vishwesh Nath, Yucheng Tang, Dong Yang, Holger R Roth, and Daguang Xu. Swin unetr: Swin transformers for semantic segmentation of brain tumors in mri images. In *International MICCAI Brainlesion Workshop*, pages 272–284. Springer, 2021.
- Ali Hatamizadeh, Yucheng Tang, Vishwesh Nath, Dong Yang, Andriy Myronenko, Bennett Landman, Holger R Roth, and Daguang Xu. Unetr: Transformers for 3d medical image segmentation. In *Proceedings of the IEEE/CVF winter conference on applications of computer vision*, pages 574–584, 2022.
- Kaiming He, Xiangyu Zhang, Shaoqing Ren, and Jian Sun. Deep residual learning for image recognition. In *Proceedings of the IEEE conference on computer vision and pattern recognition*, pages 770–778, 2016.
- Gerd Heilemann, Lukas Zimmermann, Raphael Schotola, Wolfgang Lechner, Marco Peer, Joachim Widder, Gregor Goldner, Dietmar Georg, and Peter Kuess. Generating deliverable dicom rt treatment plans for prostate vmat by predicting mlc motion sequences with an encoder-decoder network. *Medical Physics*, 2023.
- Diederik P Kingma and Jimmy Ba. Adam: A method for stochastic optimization. *arXiv preprint arXiv:1412.6980*, 2014.
- A Kyroudi, K Petersson, E Ozsahin, J Bourhis, F Bochud, and R Moeckli. Exploration of clinical preferences in treatment planning of radiotherapy for prostate cancer using pareto fronts and clinical grading analysis. *Physics and imaging in radiation oncology*, 14:82–86, 2020.
- Shuolin Liu, Jingjing Zhang, Teng Li, Hui Yan, and Jianfei Liu. A cascade 3d u-net for dose prediction in radiotherapy. *Medical physics*, 48(9):5574–5582, 2021a.
- Ze Liu, Yutong Lin, Yue Cao, Han Hu, Yixuan Wei, Zheng Zhang, Stephen Lin, and Baining Guo. Swin transformer: Hierarchical vision transformer using shifted windows. In *Proceedings of the IEEE/CVF international conference on computer vision*, pages 10012–10022, 2021b.
- M Mashayekhi, R McBeth, D Nguyen, SB Jiang, and MH Lin. Artificial intelligence guided physician directive improves head and neck planning quality and practice uniformity: a prospective study. *International Journal of Radiation Oncology, Biology, Physics*, 111(3):S44, 2021.
- Lei Mou, Yitian Zhao, Huazhu Fu, Yonghuai Liu, Jun Cheng, Yalin Zheng, Pan Su, Jianlong Yang, Li Chen, Alejandro F. Frangi, Masahiro Akiba, and Jiang Liu. Cs2-net: Deep learning segmentation of curvilinear structures in medical imaging. *Medical Image Analysis*, 67:101874, 2021. ISSN 1361-8415. doi: <https://doi.org/10.1016/j.media.2020>.

101874. URL <https://www.sciencedirect.com/science/article/pii/S1361841520302383>.
- Andriy Myronenko. 3d mri brain tumor segmentation using autoencoder regularization. In *Brainlesion: Glioma, Multiple Sclerosis, Stroke and Traumatic Brain Injuries: 4th International Workshop, BrainLes 2018, Held in Conjunction with MICCAI 2018, Granada, Spain, September 16, 2018, Revised Selected Papers, Part II 4*, pages 311–320. Springer, 2019.
- Dan Nguyen, Azar Sadeghnejad Barkousaraie, Chenyang Shen, Xun Jia, and Steve Jiang. Generating pareto optimal dose distributions for radiation therapy treatment planning. In *Medical Image Computing and Computer Assisted Intervention—MICCAI 2019: 22nd International Conference, Shenzhen, China, October 13–17, 2019, Proceedings, Part VI 22*, pages 59–67. Springer, 2019a.
- Dan Nguyen, Xun Jia, David Sher, Mu-Han Lin, Zohaib Iqbal, Hui Liu, and Steve Jiang. 3d radiotherapy dose prediction on head and neck cancer patients with a hierarchically densely connected u-net deep learning architecture. *Physics in medicine & Biology*, 64(6):065020, 2019b.
- Dan Nguyen, Troy Long, Xun Jia, Weiguo Lu, Xuejun Gu, Zohaib Iqbal, and Steve Jiang. A feasibility study for predicting optimal radiation therapy dose distributions of prostate cancer patients from patient anatomy using deep learning. *Scientific reports*, 9(1):1076, 2019c.
- Dan Nguyen, Rafe McBeth, Azar Sadeghnejad Barkousaraie, Gyanendra Bohara, Chenyang Shen, Xun Jia, and Steve Jiang. Incorporating human and learned domain knowledge into training deep neural networks: a differentiable dose-volume histogram and adversarial inspired framework for generating pareto optimal dose distributions in radiation therapy. *Medical physics*, 47(3):837–849, 2020.
- Ozan Oktay, Jo Schlemper, Loic Le Folgoc, Matthew Lee, Mattias Heinrich, Kazunari Misawa, Kensaku Mori, Steven McDonagh, Nils Y Hammerla, Bernhard Kainz, et al. Attention u-net: Learning where to look for the pancreas. *arXiv preprint arXiv:1804.03999*, 2018.
- Karl Otto. Volumetric modulated arc therapy: Imrt in a single gantry arc. *Medical physics*, 35(1):310–317, 2008.
- Yanwei Pang, Yazhao Li, Jianbing Shen, and Ling Shao. Towards bridging semantic gap to improve semantic segmentation. In *Proceedings of the IEEE/CVF International Conference on Computer Vision*, pages 4230–4239, 2019.
- David J Sher, Andrew Godley, Yang Park, Colin Carpenter, Marc Nash, Hasti Hesami, Xinran Zhong, and Mu-Han Lin. Prospective study of artificial intelligence-based decision support to improve head and neck radiotherapy plan quality. *Clinical and translational radiation oncology*, 29:65–70, 2021.
- Amber L Simpson, Michela Antonelli, Spyridon Bakas, Michel Bilello, Keyvan Farahani, Bram Van Ginneken, Annette Kopp-Schneider, Bennett A Landman, Geert Litjens, Bjoern Menze, et al. A large annotated medical image dataset for the development and evaluation of segmentation algorithms. *arXiv preprint arXiv:1902.09063*, 2019.
- Mumtaz Hussain Soomro, Victor Gabriel Leandro Alves, Hamidreza Nourzadeh, and Jeffrey V Siebers. Deepdosenet: A deep learning model for 3d dose prediction in radiation therapy. *arXiv preprint arXiv:2111.00077*, 2021.
- Yucheng Tang, Dong Yang, Wenqi Li, Holger R Roth, Bennett Landman, Daguang Xu, Vishwesh Nath, and Ali Hatamizadeh. Self-supervised pre-training of swin transformers for 3d medical image analysis. In *Proceedings of the IEEE/CVF Conference on Computer Vision and Pattern Recognition*, pages 20730–20740, 2022.
- Haojia Wang, Xicheng Chen, Rui Yu, Zeliang Wei, Tianhua Yao, Chengcheng Gao, Yang Li, Zhenyan Wang, Dong Yi, and Yazhou Wu. E-du: Deep neural network for multimodal medical image segmentation based on semantic gap compensation. *Computers in Biology and Medicine*, 151:106206, 2022.
- Binbin Wu, Francesco Ricchetti, Giuseppe Sanguineti, Misha Kazhdan, Patricio Simari, Ming Chuang, Russell Taylor, Robert Jacques, and Todd McNutt. Patient geometry-driven information retrieval for imrt treatment plan quality control. *Medical physics*, 36(12):5497–5505, 2009.

Appendix A. Tables

Table 3: R_{VA} by Structure for Each Architecture

Structures	Architecture	Validation R_{VA}	Test R_{VA}
Brainstem	Swin UNETR++	91.43%	92.13%
	Swin UNETR	85.75%	94.38%
	3D U-Net	71.43%	83.15%
	Attention U-Net	88.57%	91.01%
	SegResNet	80.00%	92.13%
	DynUNet	82.86%	93.26%
	HD U-net	91.43%	92.13%
	C3D	91.43%	94.38%
Spinal Cord	Swin UNETR++	89.47%	95.45%
	Swin UNETR	84.21%	95.45%
	3D U-Net	86.84%	94.32%
	Attention U-Net	92.11%	94.32%
	SegResNet	92.11%	89.77%
	DynUNet	86.84%	95.45%
	HD U-net	94.74%	96.59%
	C3D	94.74%	93.18%
Right Parotid	Swin UNETR++	82.5%	86.87%
	Swin UNETR	92.50%	82.83%
	3D U-Net	55.00%	50.51%
	Attention U-Net	92.50%	76.77%
	SegResNet	77.50%	75.76%
	DynUNet	82.50%	85.85%
	HD U-net	90.00%	87.87%
	C3D	82.50%	85.86%
Left Parotid	Swin UNETR++	84.21%	88.78%
	Swin UNETR	78.95%	95.71%
	3D U-Net	78.94%	63.27%
	Attention U-Net	81.58%	76.53%
	SegResNet	78.94%	75.51%
	DynUNet	73.68%	77.55%
	HD U-net	94.74%	81.63%
	C3D	89.47%	85.71%
Esophagus	Swin UNETR++	94.12%	79.07%
	Swin UNETR	100.00%	83.72%
	3D U-Net	88.24%	72.09%
	Attention U-Net	82.35%	67.44%
	SegResNet	82.35%	69.77%
	DynUNet	76.47%	69.77%
	HD U-net	82.35%	76.74%
	C3D	88.24%	83.72%

Table 4: R_{VA} by Structure for Each Architecture (continued from Table 3)

Structures	Architecture	Validation R_{VA}	Test R_{VA}
Larynx	Swin UNETR++	77.27%	84.91%
	Swin UNETR	86.36%	73.58%
	3D U-Net	45.45%	52.83%
	Attention U-Net	81.82%	75.47%
	SegResNet	59.09%	75.47%
	DynUNet	72.72%	81.13%
	HD U-net	86.36%	77.36%
	C3D	68.18%	73.58%
Mandible	Swin UNETR++	82.14%	83.33%
	Swin UNETR	85.71%	86.11%
	3D U-Net	42.86%	54.16%
	Attention U-Net	75.00%	83.33%
	SegResNet	67.86%	79.17%
	DynUNet	78.57%	88.89%
	HD U-net	82.14%	87.50%
	C3D	75.00%	83.33%
PTV56	Swin UNETR++	97.37%	97.80%
	Swin UNETR	94.74%	96.70%
	3D U-Net	84.21%	72.53%
	Attention U-Net	97.37%	96.70%
	SegResNet	89.47%	97.80%
	DynUNet	97.37%	97.80%
	HD U-net	97.37%	96.70%
	C3D	94.74%	92.31%
PTV63	Swin UNETR++	92.31%	97.62%
	Swin UNETR	92.31%	92.86%
	3D U-Net	65.38%	61.90%
	Attention U-Net	88.46%	83.33%
	SegResNet	84.61%	90.48%
	DynUNet	88.46%	80.95%
	HD U-net	96.15%	88.10%
	C3D	92.31%	90.48%
PTV70	Swin UNETR++	95.00%	99.00%
	Swin UNETR	92.50%	98.00%
	3D U-Net	65.00%	57.00%
	Attention U-Net	82.50%	87.00%
	SegResNet	85.00%	96.00%
	DynUNet	85.00%	88.00%
	HD U-net	97.50%	94.00%
	C3D	92.50%	94.00%

Appendix B. Result Visualizations

Figure 3: 3D dose estimation on test patient No.241 from each architecture

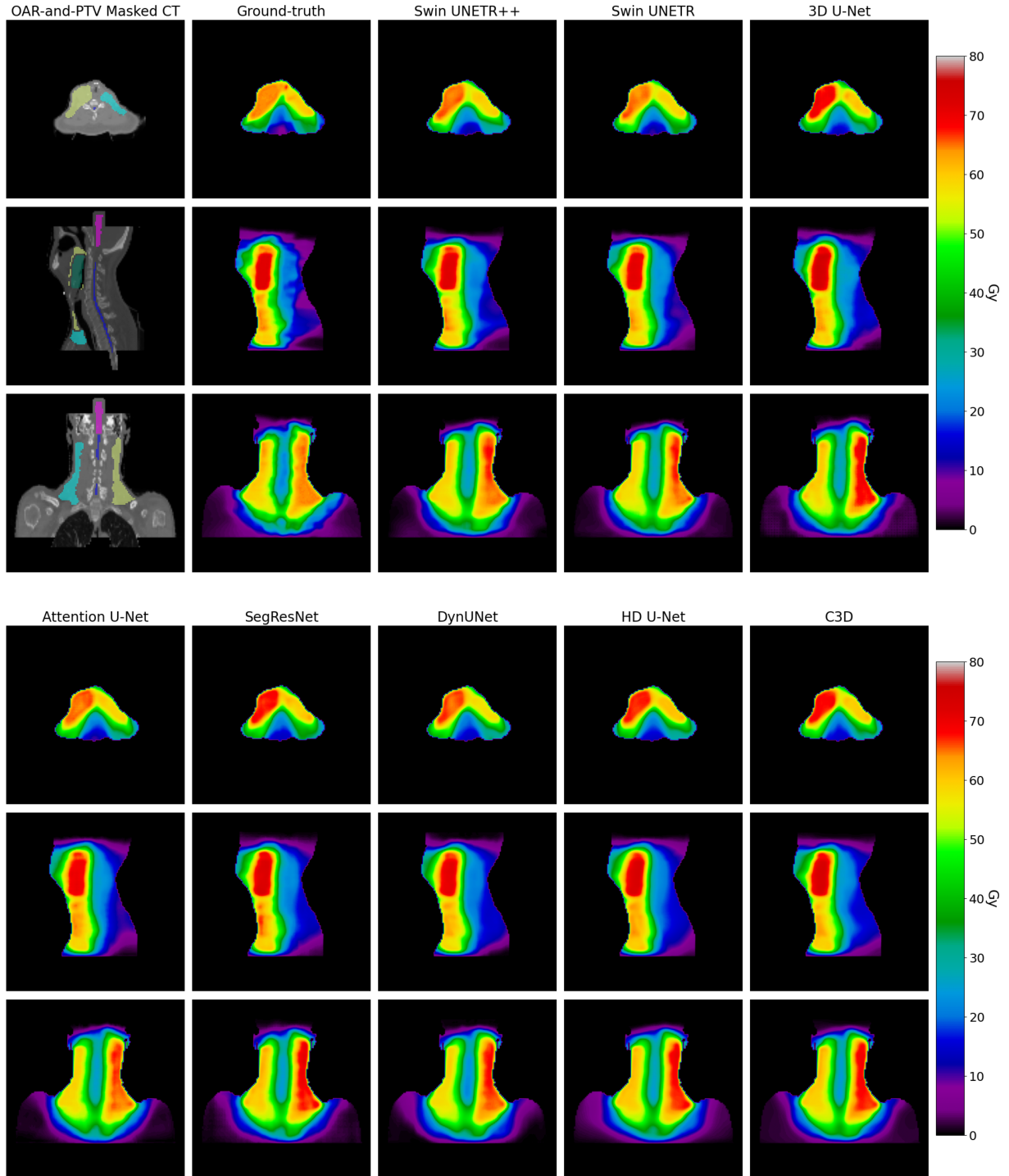


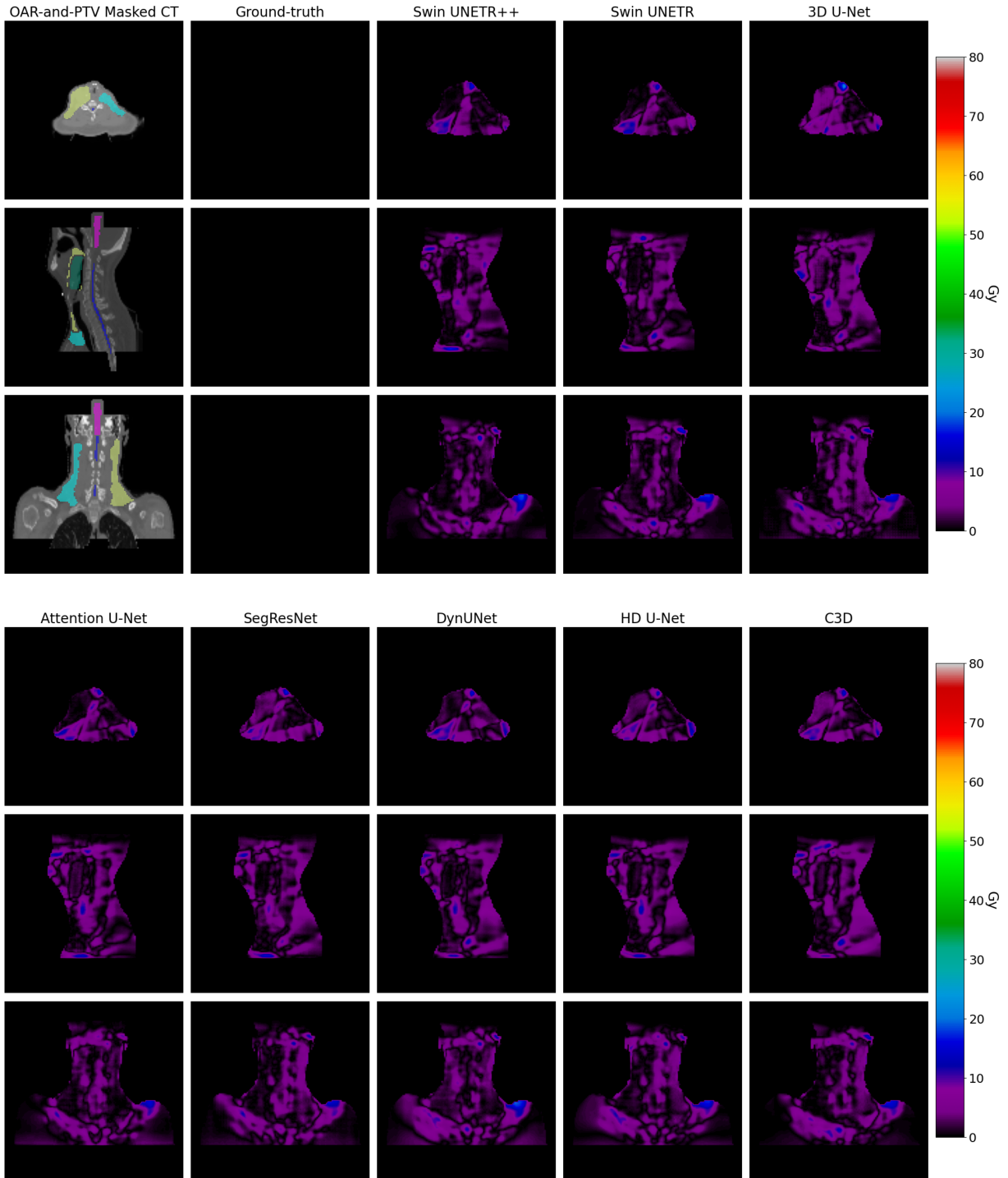
Figure 4: $|D_{\text{pred}} - D_{\text{gt}}|$ for test patient No.241 from each architecture

Figure 5: DVH: predicted (dashed) vs ground-truth (solid) for test patient No.241 from each architecture

